

## Numerical modeling of pore-scale phenomena during CO<sub>2</sub> sequestration in oceanic sediments

Qinjun Kang, Ioannis N. Tsimpanogiannis\*,  
Dongxiao Zhang, Peter C. Lichtner

*Hydrology, Geochemistry and Geology Group (EES-6), Los Alamos National Laboratory,  
MS T003, Los Alamos, NM 87545, United States*

---

### Abstract

Direct disposal of liquid CO<sub>2</sub> on the ocean floor is one of the approaches considered for sequestering CO<sub>2</sub> in order to reduce its concentration in the atmosphere. At oceanic depths deeper than approximately 3000 m, liquid CO<sub>2</sub> density is higher than the density of seawater and CO<sub>2</sub> is expected to sink and form a pool at the ocean floor. In addition to chemical reactions between CO<sub>2</sub> and seawater to form hydrate, fluid displacement is also expected to occur within the ocean floor sediments. In this work, we consider two different numerical models for hydrate formation at the pore scale. The first model consists of the Lattice Boltzmann (LB) method applied to a single-phase supersaturated solution in a constructed porous medium. The second model is based on the Invasion Percolation (IP) in pore networks, applied to two-phase immiscible displacement of seawater by liquid CO<sub>2</sub>. The pore-scale results are upscaled to obtain constitutive relations for porosity, both transverse and for the entire domain, and for permeability. We examine deposition and displacement patterns, and changes in porosity and permeability due to hydrate formation, and how these properties depend on various parameters including a parametric study of the effect of hydrate formation kinetics. According to the simulations, the depth of CO<sub>2</sub> invasion in the sediments is controlled by changes in the pore-scale porosity close to the hydrate formation front.

© 2005 Elsevier B.V. All rights reserved.

**Keywords:** Oceanic CO<sub>2</sub> sequestration; Hydrate formation; Pore network; Lattice Boltzmann; Invasion Percolation

---

---

\* Corresponding author. Tel.: +1 505 667 9190; fax: +1 505 665 8737.

E-mail address: ioannis@lanl.gov (I.N. Tsimpanogiannis).

## 1. Introduction

The release of  $\text{CO}_2$  to the atmosphere has attracted significant scientific interest because of its impact on global warming. Various disposal methods (oceanic, oil reservoirs, saline aquifers, etc.) are currently under consideration to sequester  $\text{CO}_2$ . Direct disposal of liquid  $\text{CO}_2$  on the sea floor is one of the approaches being considered for oceanic disposal of  $\text{CO}_2$  (e.g., see Fig. 1). An extensive list of papers examining the aforementioned approaches can be found in the special issues of *Energy Conversion Management* vol. 38 (supplement), 1997; vol. 37 (6–8), 1996; vol. 36 (6–9), 1995; vol. 34 (9–11), 1993, and vol. 33 (5–8), 1992. As the density of liquid  $\text{CO}_2$  is higher than that of seawater for depths below approximately 3000 m, the liquid  $\text{CO}_2$  is expected to initially create a pool on the ocean floor. In a further step liquid  $\text{CO}_2$  could displace the seawater saturating the sediments through a gravity-driven flow. A number of interesting physical and chemical phenomena can occur in the vicinity of the carbon dioxide/seawater interface including, among others, counter-current diffusion of the two phases, mass transfer due to convection in the presence of ocean currents, aqueous chemical reactions, salting out effects, etc. If appropriate temperature and pressure conditions are present, a hydrate film forms at the interface of seawater and the liquid  $\text{CO}_2$  pool, which slows down the diffusion process. Hydrates are crystalline structures formed by hydrogen-bonded water molecules that form a cage containing cavities which can be stabilized by the presence of gas molecules such as carbon dioxide [1,2]. It has been theoretically demonstrated and experimentally observed that hydrate formation is not restricted to a thin layer close to the gas–liquid interface but can occur anywhere in the liquid water phase if the solution is supersaturated [3,4].

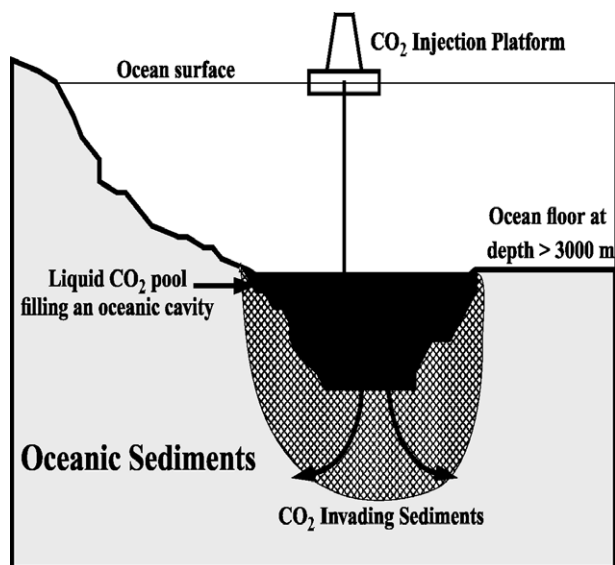


Fig. 1. Carbon dioxide disposal scheme at the ocean floor.

However, the formation mechanism is still not fully understood, especially in porous media. These processes could modify the porosity and permeability of the ocean floor sediments, as well as its composition, thus affecting how deep the liquid CO<sub>2</sub> can penetrate into the sediments.

In this work, we have utilized two pore-scale methods, LB [5] and IP [6,7] in pore networks. These modeling methods can enhance the understanding of phenomena at the pore scale and provide constitutive relations for macroscale continuum models. In addition, the pore-scale models could determine if upscaling to the continuum scale is possible. We have simulated numerically hydrate formation in porous media from a single-phase supersaturated solution using the LB method, and from two-phase immiscible displacement of seawater by liquid CO<sub>2</sub> using the IP method in pore networks.

In recent years, the LB method has been developed into a promising numerical scheme for simulating flows and modeling physics and chemistry in complex fluids at the pore scale. Unlike conventional numerical schemes based on discretizations of macroscopic continuum equations, the LB method is based on a discrete representation of fluids via particle movement on a lattice [5]. This feature gives the LB method the advantage of studying non-equilibrium dynamics, especially in fluid flow applications involving interfacial dynamics and complex boundaries (geometries). Since its appearance, the LB method has been successfully applied to studying a variety of flow and transport phenomena such as flow in porous media, turbulence, multiphase and multicomponent flows, particles suspended in fluids, and heat transfer and reaction–diffusion [5]. Recently, Kang et al. [8,9] have developed an LB model for simulating dissolution and/or precipitation in porous media. This model was extended in a previous study to the simulation of crystal formation from a supersaturated solution based on a first-order kinetic rate law and in the absence of fluid flow [10]. The effect of Peclet number ( $Pe$ , the ratio of convection to diffusion) and the second Damkohler number ( $Da_{II}$ , the ratio of reaction to diffusion) are examined. In this study, we apply this model to the numerical simulation of hydrate formation from dissolved CO<sub>2</sub> during its sequestration in oceanic sediments.

Percolation theory and its variant IP in pore networks have contributed significantly in enhancing our understanding of phenomena occurring within porous media. Pore networks have primarily been used to study two-phase or multi-phase displacement processes in porous media after their introduction by the pioneering work of Fatt [11]. Excellent reviews have been provided by Feder [6], Sahimi [7], Blunt and coworkers [12,13]. Primarily, pore networks have been used to calculate relative permeabilities, electrical resistivities and capillary pressures, the effects of gravity and viscous forces, and the effects of spatial correlation, and wettability. In recent years, pore networks have also been used to study mass transfer processes such as solution gas drive [14,15], drying [16,17], boiling [18], and the critical gas saturation during primary oil production [19,20]. In the second part of this study, where we examine IP in pore networks, we combine a two-phase displacement with a phase change (liquid to solid) process and examine parametrically the effect of hydrate formation kinetics on the liquid carbon dioxide invasion patterns observed, as well as the change of porosity of the system as a result of pore blocking due to hydrate formation.

## 2. Model development

### 2.1. Lattice Boltzmann method

Here, we give a brief introduction to the LB method. Interested readers may refer to previous publications for more details [8–10]. In the LB method, fluid flow can be simulated with the following Lattice BGK equation:

$$f_i(\mathbf{x} + \mathbf{e}_i \delta_t, t + \delta_t) = f_i(\mathbf{x}, t) - \frac{f_i(\mathbf{x}, t) - f_i^{\text{eq}}(\rho, \mathbf{u})}{\tau}, \quad (1)$$

where  $f_i$  is the particle velocity distribution function along the  $i$  direction,  $\delta_t$  is the time increment,  $\tau$  is the relaxation time,  $\rho$  and  $\mathbf{u}$  are the density and velocity of the fluid, calculated using  $\rho = \sum_i f_i$  and  $\rho \mathbf{u} = \sum_i \mathbf{e}_i f_i$ , respectively,  $\mathbf{e}_i$ s are the discrete velocities, and  $f_i^{\text{eq}}$  is the corresponding equilibrium distribution function. In the most commonly used two-dimensional, nine-speed (D2Q9) model,  $\mathbf{e}_i$ s have the following form:

$$\mathbf{e}_i = \begin{cases} 0 & i = 0, \\ \left( \cos \frac{(i-1)\pi}{2}, \sin \frac{(i-1)\pi}{2} \right) & i = 1 - 4, \\ \sqrt{2} \left( \cos \left[ \frac{(i-5)\pi}{2} + \frac{\pi}{4} \right], \sin \left[ \frac{(i-5)\pi}{2} + \frac{\pi}{4} \right] \right) & i = 5 - 8, \end{cases} \quad (2)$$

$\tau$  is related to the kinematic viscosity by  $\nu = 1/3 (\tau - 1/2)$ , and  $f_i^{\text{eq}}$  has the following form:

$$f_i^{\text{eq}}(\rho, \mathbf{u}) = \omega_i \rho \left[ 1 + 3 \mathbf{e}_i \cdot \mathbf{u} + \frac{9(\mathbf{e}_i \cdot \mathbf{u})^2}{2} - \frac{3\mathbf{u}^2}{2} \right], \quad (3)$$

where  $\omega_i$ s are the associated weight coefficients, which are  $\omega_0 = 4/9$ ,  $\omega_i = 1/9$  for  $i = 1, 2, 3, 4$ , and  $\omega_i = 1/36$  for  $i = 5, 6, 7, 8$ .

It is well known that, using the Chapman–Enskog expansion, one can prove that the above LB equation, Eq. (1), recovers the correct continuity and momentum equations at the Navier–Stokes level [21,22].

$$\frac{\partial \rho}{\partial t} + \nabla \cdot (\rho \mathbf{u}) = 0, \quad (4)$$

$$\frac{\partial (\rho \mathbf{u})}{\partial t} + \nabla \cdot (\rho \mathbf{u} \mathbf{u}) = - \nabla p + \nabla \cdot [\rho \nu (\nabla \mathbf{u} + (\nabla \mathbf{u})^\top)], \quad (5)$$

where  $p = 1/3 \rho$  is the fluid pressure.

In our study, we assume that the solute concentration does not affect the density and velocity of the solution. As a result, the solute transport can be described by another distribution function, which satisfies a similar evolution equation as  $f_i$ . This evolution equation can be proved to recover the convection–diffusion equation [23].

We consider the general first-order kinetic reaction model at the fluid–solid interface:

$$D \frac{\partial C}{\partial n} = k_r (C - C_s), \quad (6)$$

where  $D$  is the diffusivity,  $C$  is the solute concentration at the interface,  $C_s$  is the saturated concentration,  $k_r$  is the local reaction rate constant, and  $n$  is the direction normal to the interface pointing toward the fluid phase. This reaction model is very similar to the kinetic models for hydrate formation proposed by Englezos et al. [24] and by Bishnoi and Natarajan [25]. The driving force in their model is the difference between the fugacity of the dissolved gas and its fugacity at the three-phase equilibrium which corresponds to the concentration difference ( $\Delta C = C - C_s$ ) in our study.

The above formulation of kinetic reaction imposes a boundary condition for the solute concentration. In previous studies, we have formulated a boundary condition for the distribution function [8–10].

In this work, we neglect solute diffusion in the solid phase. Since the mechanism of hydrate nucleation is still not understood and needs to be experimentally studied [25], we assume that hydrate crystal growth only occurs at the liquid–solid interface, even though clathrates were often found to form within the center of pore spaces, rather than on grain surfaces [3,4]. In this study, each node at the interface represents a control volume with a size of  $1 \times 1$  (in lattice units) and is located at the center of this volume. As can be seen from Fig. 2, node  $Q$  is the center of the control volume surrounded by dashed lines. The initial control volume is given a mass  $b_0$ . We update the mass at each time step by  $b = b + \Delta x k_r (C - C_s) \delta t = b + k_r (C - C_s)$ , where  $\Delta x$  is the length of the control volume along the interface and  $\delta t$  is the time increment. In this case, they both equal unity. For a control volume, when  $b = 2b_0$ , i.e., when the mass doubles, one of the nearest ( $S$ ) or diagonal non-solid nodes ( $R$  and  $T$ ) becomes a solid particle with a probability of  $\mathcal{P}_S = 4\mathcal{P}_R = 4\mathcal{P}_T$ . The ratio of solidification probability between the nearest node and diagonal nodes is 4:1, which equals the ratio of weight coefficients between the vertical ( $e_2$ ) and diagonal directions ( $e_5$  and  $e_6$ ). The criterion ( $b = 2b_0$ ) for converting a non-solid node to a solid one is not unique. In general, we can add  $n - 1$  solid nodes when  $b = nb_0$ , where  $n \leq m + 1$  ( $m$  is the number of the neighboring non-solid nodes). However,  $n = 2$  is the most convenient and straightforward way. Adding more than one node each time ( $n \geq 3$ ) may introduce larger discrete error and thus leads to different morphologies.

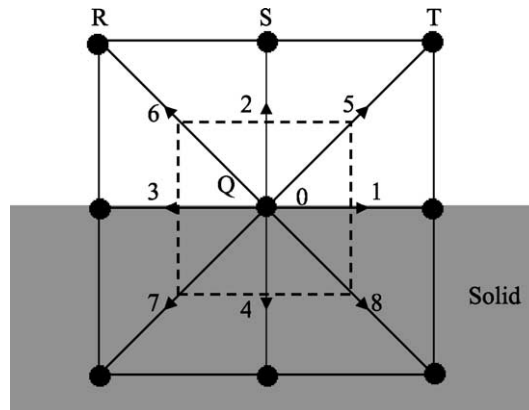


Fig. 2. Schematic illustration of a wall node.

## 2.2. Invasion Percolation in pore networks

IP has been used extensively to model the slow immiscible displacement, controlled by capillary forces, of two phases within a porous medium (a non-wetting phase displacing a wetting phase) [26]. In this approach, the porous medium is replaced by a lattice of sites (representing pores) and bonds (representing throats). Both pores and throats can be distributed following an appropriate size distribution. In the absence of gravity or viscous forces (in other words, when there is no spatial or time dependence of the invasion threshold), this process is known to produce self-similar fractal patterns that resemble an ordinary percolation cluster. On the other hand, if gravity and/or viscous forces are important, the invasion threshold has a gradient in space and that is known to produce self-affine fronts which have a characteristic finite width [27,28].

Consider a geological porous medium (e.g., oceanic sediment) which is initially fully saturated with liquid water. In the more general case, electrolytes are present within the sediments as well, however, their effects are ignored for this preliminary study. At the upper boundary of the porous medium, a pool of  $\text{CO}_2$  is placed.

A pore network representation is assumed in the form of a regular periodic lattice of size  $N \times M$ , a special case of which is  $N=M$ . The lattice sites (pores) provide the storage capacity of the network, while the lattice bonds (throats) connecting neighboring sites provide the resistance to flow. A typical schematic of such a network is depicted in Fig. 3. Both pores and throats can be randomly distributed and uncorrelated. Usually, sites are taken to be spherical while bonds are cylindrical. Application of the methodology to more realistic geometries such as using square or triangular throats is straightforward, although more computationally demanding. One can use reported experimental values of pores/throats that correspond to oceanic sediments (see, for example, [29], for the case of methane hydrate dissociation) to reconstruct a more realistic porous medium. Here, however, a more simplified approach

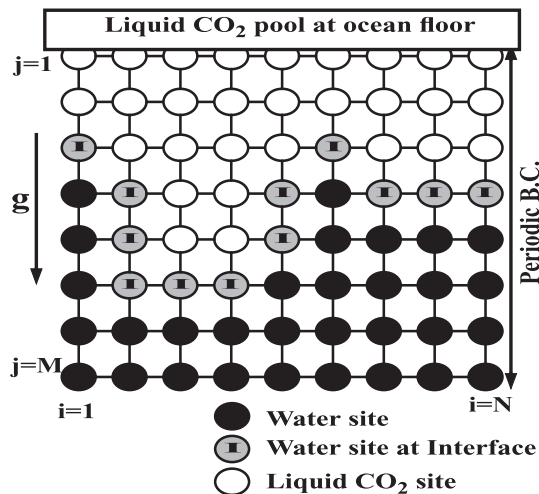


Fig. 3. Schematic of a square ( $N \times M$ ) site-bond lattice.

was considered. In addition, it is assumed that the throats have an invasion threshold  $\pi_j$  given in the general case by the relation:

$$\pi_j = \tau_j + Bz_j, \quad (7)$$

and

$$B = \frac{g(\rho_w - \rho_{nw})k}{\gamma}, \quad (8)$$

where  $z_j$  is the depth (in lattice units) of site  $j$  ( $z_j$  is increasing downward), and  $\tau_j$  is a random number from a uniform distribution on the unit interval. The introduction of randomness into  $\pi_j$  reflects the randomness of capillary thresholds of the throats. This approach is followed in order to capture the disorder (in throat sizes) of the oceanic sediments.  $B$  is the Bond number (describes the competition between gravity and capillary forces),  $g$  is the component of gravity in the displacement direction,  $\rho$  is the density, subscripts  $w$  and  $nw$  denote wetting ( $H_2O$ ) and non-wetting ( $CO_2$ ) phases, respectively,  $k$  is the permeability of the porous medium, and  $\gamma$  is the interfacial tension between the fluids. For the problem of interest, we estimated that at oceanic depth of 3000 m ( $T=274.65$  K and  $P=30$  MPa) the Bond number is  $B \approx (-10^{-13}) - (-10^{-17})$  (lower values of  $B$  are obtained for sediments with lower permeability). For the calculation of Bond number, the following parameters were used:  $\rho_w=1041.0$  kg/m<sup>3</sup> [30],  $\rho_{nw}=1049.3$  kg/m<sup>3</sup> [31],  $\gamma=29.0$  mN/m [32], and  $k=10^{-17}-10^{-21}$  m<sup>2</sup> that corresponds to mudstones from the Norwegian margin [33]. During invasion, we select to invade throats with minimum thresholds  $\pi_j$ . Because  $B < 0$  (recall that  $\rho_w < \rho_{nw}$  for the conditions of interest to this study), the non-wetting phase ( $CO_2$ ) tends to grow toward throats with larger  $z$  (deeper in the sediments). As a result, this is expected to favor throats that are further advanced in the direction parallel to the gravity vector. This process eventually produces invasion patterns that are consistent with Invasion Percolation in a Destabilizing Gradient (IPDG). Due to the very small Bond number in our simulation, a significant effect of gravity occurs only if large networks are used ( $N \sim 10^{13}-10^{17}$ ). Thus, since our study is limited to smaller size networks,  $B=0$  is used for the remainder of the study which is expected to give same patterns as if using  $B \ll 1$ .

The simulation algorithm consists of two distinct steps: invasion and hydrate formation (reaction). The numerical simulation for the first step proceeds as follows: initially all the lattice sites are filled with water, which is the “defending” phase in the system, while liquid  $CO_2$  is the “invading” phase. Periodic boundary conditions are used in the directions perpendicular to the gravity gradient. A line injection scheme is considered along the entire top boundary of the network ( $z_j=1$ ) which is invaded by liquid  $CO_2$ . Alternatively, one could consider a point injection scheme which would resemble more closely the case of injecting through a well. An interface develops within the pore network that separates water occupied sites from liquid  $CO_2$  sites. A water site belongs to the interface (denoted as *I-site*) if at least one closest neighbor site is a liquid  $CO_2$  occupied site. As a first step in the process, all water sites that belong to that interface (invasion front) are identified along with the corresponding throats. Once the invasion front is identified, we select to invade next the throat (and the respective connected pore to that throat) with the least invasion



threshold. To take into account the incompressibility of the two phases involved in the process, trapping rules are considered [34]. The displaced phase is considered trapped if it is completely surrounded by the invading phase and cannot be moved any further by the invading phase. Identification of the trapped water clusters is performed by using the well-known Hoshen–Kopelman algorithm [35].

Next the reaction step is described. It is assumed that below a certain depth  $z_H$  within the network, such that,  $2 < z_H < M$  (recall that the first row in the network is always occupied with  $\text{CO}_2$  acting as the supply pool), the hydrate stability zone (HSZ) exists satisfying the condition:  $T \leq T_d$  and  $P \geq P_d$ , where  $T_d$  and  $P_d$  are the equilibrium hydrate formation temperature and pressure, respectively. In real oceanic sediments, the HSZ corresponds to a zone that can be several hundred meters deep, where the temperature and pressure are such that hydrate formation can occur. Outside that zone hydrate dissociates into two phases. The thickness of the HSZ depends on several factors including the geothermal gradient, the average temperature of the liquid  $\text{CO}_2$  pool/oceanic sediment interface and ocean depth [36].

Thus, once liquid carbon dioxide reaches the HSZ, hydrate formation can occur. Of importance to the process is the hydrate formation reaction rate and the characteristic time for reaction compared to the characteristic time for invasion. We examine the hydrate formation process parametrically in the following way. A dimensionless number  $\lambda$  is defined which denotes the number of invasion steps performed for each reaction step. During the reaction part, initially all pores saturated with liquid carbon dioxide are identified which belong at the HSZ, and then, one of the pores to be occupied completely with hydrate is selected at random. It has been shown (e.g., by using two-dimensional, 2D, visualization experiments [3]) that during hydrate formation, all the water inside a pore can solidify into hydrate with the exception of a thin (5–50 nm) adsorbed film that remains liquid. Ice is strongly non-wetting and forms convex shapes within the pores that minimize the surface area [37]. Note, however, that alternative concepts (of where hydrate nucleates and grows) have also been reported, such as the cementation of sediment grains that results from hydrate formation [38].

Hydrate formation results in pore blocking which subsequently cannot accommodate any further flow through thereby reducing the porosity of the system. To present a simple example, consider the case with  $\lambda=4$ . In this case, liquid carbon dioxide first invades 4 sites and then one of the invaded sites is occupied with hydrate if it is in the HSZ. Smaller values of  $\lambda$  imply faster kinetics while larger values of  $\lambda$  imply slower kinetics. The limiting case when  $\lambda \rightarrow \infty$  implies that no hydrate formation occurs, whereas  $\lambda \rightarrow 1$  implies that once  $\text{CO}_2$  enters HSZ it forms hydrate immediately. In that case, a zone having a width of one lattice unit is formed and blocks any further  $\text{CO}_2$  invasion in the sediments.

### 3. Results and discussion

#### 3.1. Lattice Boltzmann simulations

The two-dimensional porous medium constructed for the LB study has a size of 108 by 90 (in lattice units). A few arrays of void space are added at both the top and bottom



boundaries. The density (pressure) is fixed at both ends and fluid flows from the top to bottom. The left and right boundaries are treated as no flow boundaries.

Initially, the pore space is filled with solution saturated with CO<sub>2</sub>. The saturation of the inflowing fluid is fixed at 1 until the flow reaches a steady state. Then the inflowing fluid is changed to a supersaturated solution with a saturation of 1.2. Hydrate precipitation then takes place. The simulation is terminated when the permeability of the medium reaches 0 due to clogging. In this study, the effect of chemical and other forces that may reopen the clogged medium is ignored.

In addition to saturation, there are two other dimensionless parameters controlling this process. They are the Peclet number  $Pe = UL/D$  and the second Damkohler number  $Da_{II} = k_r L/D$  (or the first Damkohler number,  $Da_I = k_r/U = Da_{II}/Pe$  [39]), where  $U$  is the average steady-state velocity of the fluid over the entire domain,  $L$  is the length of the system in the transverse direction, and  $D$  is the molecular diffusivity. The  $Pe$  number describes the effect of advection relative to that of molecular diffusion on solute transport and  $Da_I$  and  $Da_{II}$  describe the effect of reaction relative to that of convection and diffusion, respectively. The main focus during this study is on how these dimensionless parameters affect hydrate formation.

### 3.1.1. Effect of Damkohler numbers

Fig. 4 shows the initial and final geometries due to precipitation at  $Pe = 62.8$  and at different  $Da_{II}$  numbers. Regions in black correspond to the initial medium and regions in red depict hydrate formed. As  $Da_{II}$  decreases, the time (normalized by  $L^2/D$ ) needed to plug the medium increases. As shown in (a), hydrate formation mainly occurs at the upstream boundary for large  $Da_{II}$  numbers (fast kinetics), resulting in the quick blocking of the pore space and hence preventing the supersaturated solution from entering the medium. As the  $Da_{II}$  number decreases, the supersaturated solution penetrates further into the fractures and more hydrate is formed in the downstream part of the medium. There is no hydrate formed within the transverse channel connecting the two vertical fractures in case (a); some hydrate forms in case (b); and extensive hydrate formation occurs in cases (c) and (d) that the fracture is plugged in both cases.

Fig. 5 shows the distribution of transverse porosity of the resulting geometry along the flow direction at  $Pe = 62.8$  and at different  $Da_{II}$  numbers. Porosity is normalized by the transverse porosity of the initial geometry at the same depth, and the depth is normalized by the height of the domain. The value of the normalized porosity  $\phi_t/\phi_{t0}$  is between 0 and 1. When it equals 1, no hydrate forms at that depth; when it equals 0, the geometry is plugged at that depth. For each  $Da_{II}$  number, the transverse porosity increases with distance from the upstream boundary, because in general, less hydrate is formed downstream compared to upstream. At a position very close to the upstream boundary, the smaller the  $Da_{II}$  number, the larger the normalized porosity. However, this tendency flips over at  $Z/H \approx 0.05$ . This is so because when the  $Da_{II}$  is large (fast kinetics) hydrate forms very fast in the upstream part and clogs the medium quickly, therefore prevents the solution from penetrating into the downstream and forming hydrate there.

Constitutive relations derived from the LB method for permeability as a function of porosity (for  $Pe = 62.8$  and different  $Da_{II}$  numbers) are shown in Fig. 6. The porosity is averaged over the entire LB domain, which is considered as a representative elemental

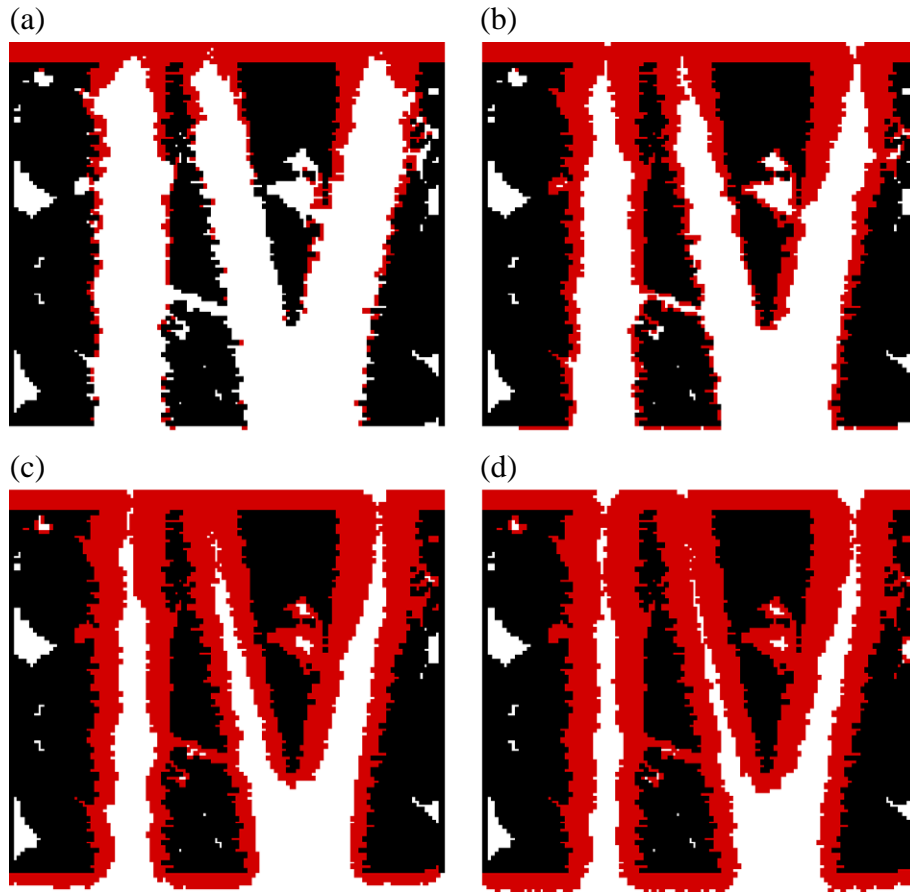


Fig. 4. Initial and resulting geometries due to precipitation at  $Pe=62.8$ : (a)  $Da_{II}=32.4$ ,  $t^*=0.0457$ ; (b)  $Da_{II}=3.24$ ,  $t^*=0.243$ ; (c)  $Da_{II}=0.324$ ,  $t^*=1.972$ ; (d)  $Da_{II}=0.0324$ ,  $t^*=17.118$ . Fluid flows from the top to the bottom. Regions in black correspond to the initial geometry and regions in red depict hydrate formed. Time  $t^*$  is normalized by  $L^2/D$ .

volume. As is evident from the figure, the permeability becomes zero even for large values of porosity due to clogging near the inlet. The threshold porosity at which the permeability vanishes increases with increasing  $Da_{II}$  number. The constitutive relation found here is quite different from the usual power-law relations often used in continuum formulations in which the permeability goes to zero at zero porosity and clogging effects are not taken into account.

### 3.1.2. Effect of Peclet number

Fig. 7 shows the initial and resulting geometries due to precipitation at  $Da_{II}=3.24$  and at different  $Pe$  numbers. As shown in (a), hydrate formation mainly occurs at the upstream boundary at a small  $Pe$  number, resulting in the quick blocking of the pore space and hence preventing the supersaturated solution from entering the medium. As the  $Pe$  number

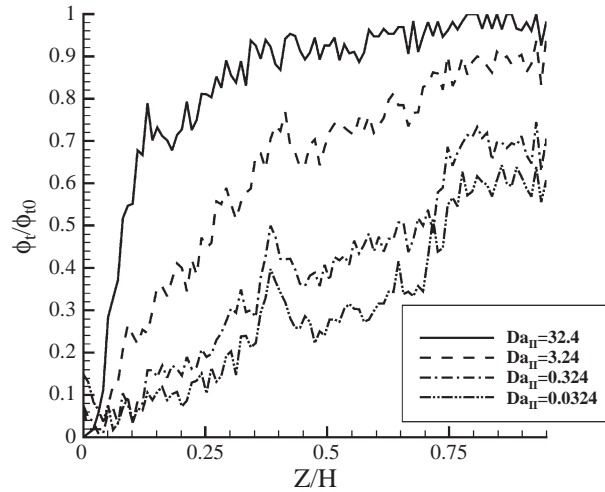


Fig. 5. Distribution of transverse porosity of the resulting geometry along the flow direction. The  $Pe$  number is 62.8. Porosity is normalized by the transverse porosity of the initial geometry at the same depth and the depth is normalized by the height of the domain  $H$ .

increases (fluid velocity increases), the supersaturated solution penetrates further into the fractures and more hydrate is formed downstream. In this sense, the  $Pe$  number plays an opposite role as the  $Da_{II}$  number. It is useful to discuss the results based on the first Damkohler number. For a large  $Da_I$  number, hydrate formation mainly occurs at the entrance. More and more hydrate is formed downstream as the  $Da_I$  number decreases. This observation is confirmed by the distribution of normalized transverse porosity along

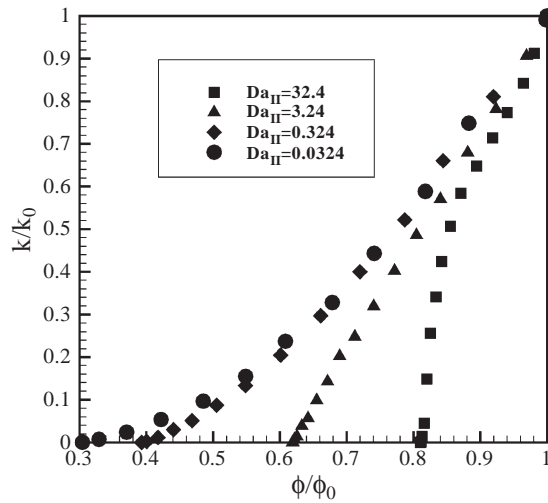


Fig. 6. Permeability–porosity relation at  $Pe=62.8$ . Both permeability and porosity are normalized by those of the initial geometry.

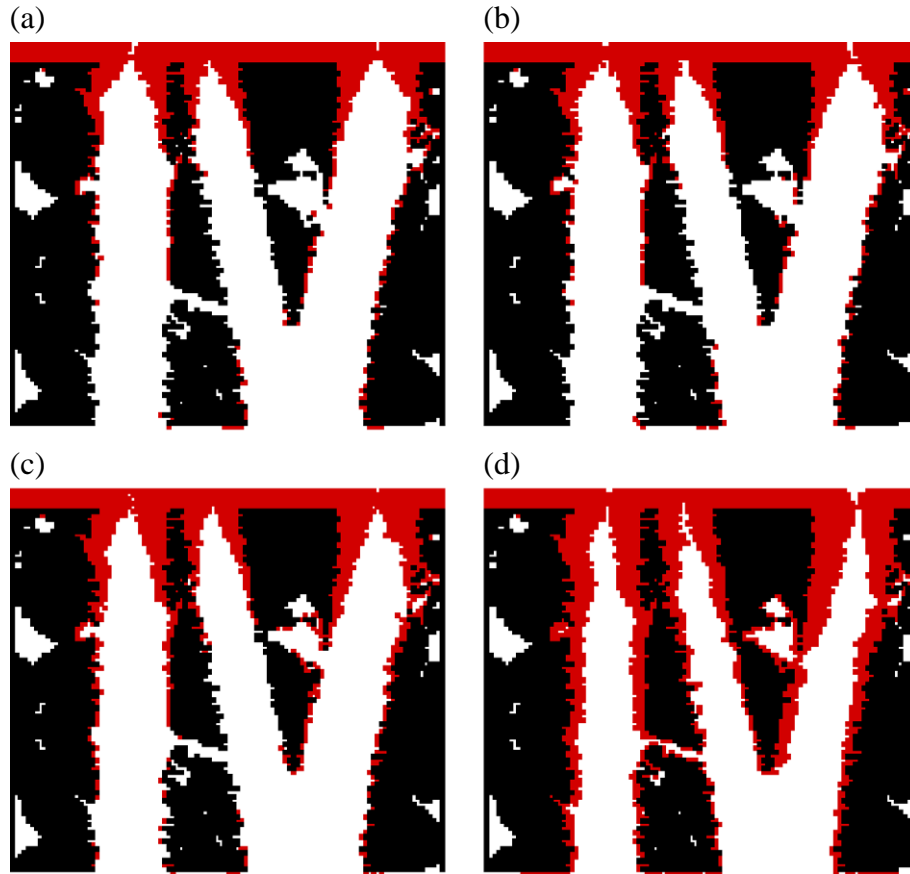


Fig. 7. Initial and resulting geometries due to precipitation at  $Da_{II}=3.24$ : (a)  $Pe=0.0628$ ,  $t^*=0.286$ ; (b)  $Pe=0.628$ ,  $t^*=0.286$ ; (c)  $Pe=6.28$ ,  $t^*=0.283$ ; (d)  $Pe=62.8$ ,  $t^*=0.243$ . Fluid flows from the top to the bottom. Regions in black correspond to the initial geometry and regions in red depict hydrate formed. Time  $t^*$  is normalized by  $L^2/D$ .

flow direction at  $Da_{II}=3.24$  and at different  $Pe$  numbers corresponding to Fig. 7, and by the corresponding permeability–porosity relation.

Since the permeability of the ocean sediments is very low [33], the  $Da_I$  number should be very large (since the  $Pe$  is very small) and hydrate tends to form extensively near the entrance, resulting in quick clogging of the medium.

### 3.2. Pore network results

Typical invasion patterns obtained from the pore network calculations for some of the different cases examined are depicted in Fig. 8. The patterns range from very fast hydrate formation kinetics (Fig. 8a) to essentially no hydrate forming conditions (Fig. 8d). Note that in the limit of fast kinetics, as  $CO_2$  entering the HSZ immediately forms hydrate, thus resulting in blocking the pore space, and the formation of a thin

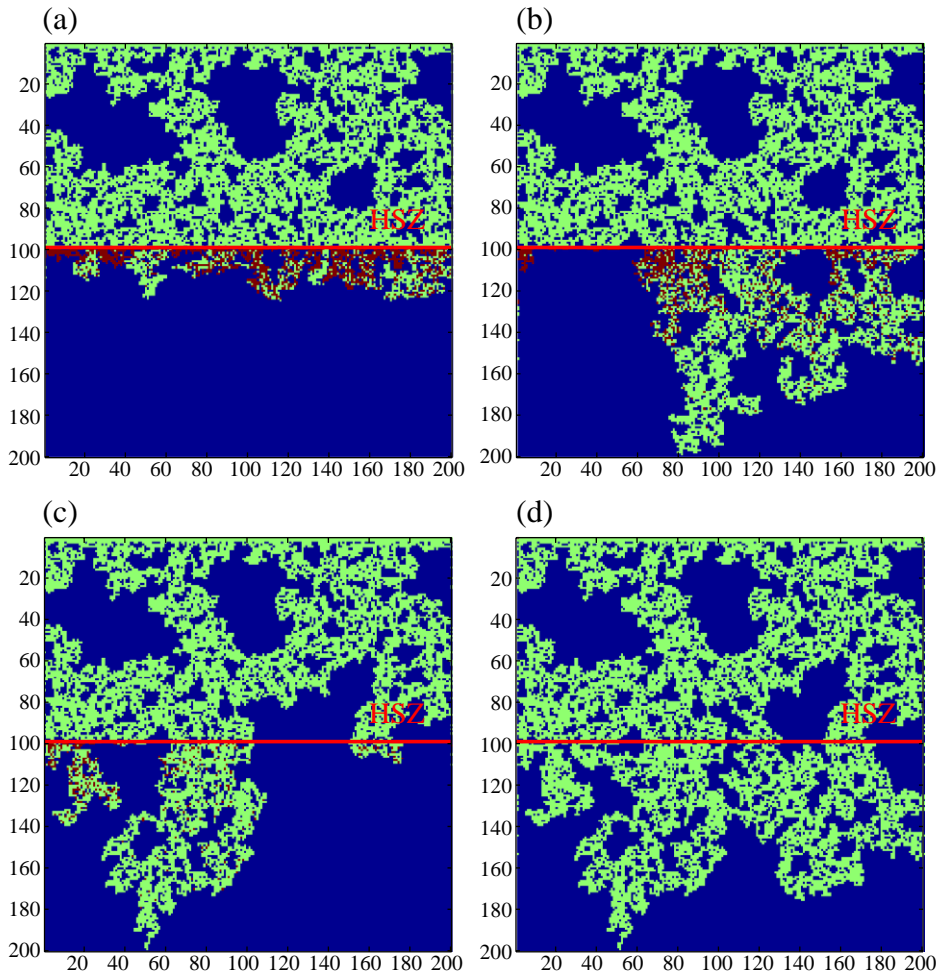


Fig. 8. The effect of reaction kinetics on the obtained CO<sub>2</sub> invasion patterns in a 200 × 200 lattice for various  $\lambda$ : (a)  $\lambda=2$ ; (b)  $\lambda=7$ ; (c)  $\lambda=15$ ; (d)  $\lambda=\infty$ . Color code: green (CO<sub>2</sub>), blue (H<sub>2</sub>O), red (CO<sub>2</sub>-hydrate). The red solid line denotes the beginning of the HSZ. Fluid flows from the top to the bottom.

layer of hydrate which does not allow any further penetration of CO<sub>2</sub> into the HSZ. As a result of the pore blocking, a pool of trapped liquid CO<sub>2</sub> is formed above the HSZ (Fig. 8a).

Fig. 9a shows the effect of  $\lambda$  on the width  $\sigma_f$  of the hydrate zone that has formed, and which is defined as

$$\sigma_f^2 = \frac{\int_0^\infty (X_{ft} - z)^2 p_f(z) dz}{\int_0^\infty p_f(z) dz}, \quad (9)$$

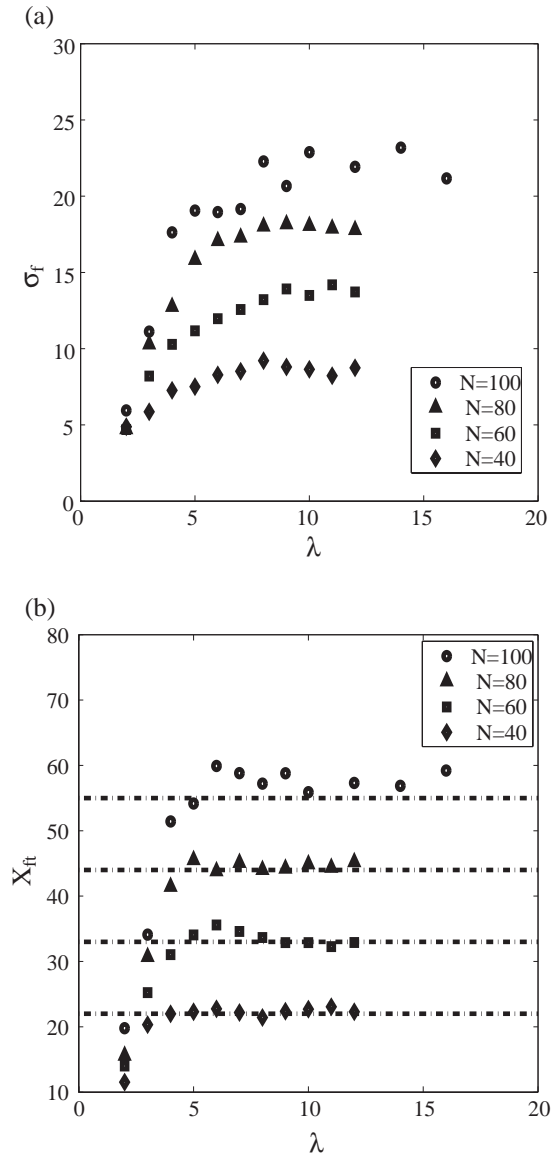


Fig. 9. The effect of  $\lambda$  on (a) the width  $\sigma_f$  of the hydrate occupied zone and, (b) the mean position of the hydrate occupied zone. The results shown depict four different  $N \times N$  lattice sizes ( $N=100, 80, 60, 40$ ). The results for each lattice size are averaged over 80 realizations. The HSZ starts at  $j=N/10$ .

where  $p_f(z)$  is the probability of finding one site occupied by hydrate at  $z$ , and  $X_{ft}$  is the mean position of the hydrate zone defined as

$$X_{ft} = \frac{\int_0^\infty zp_f(z)dz}{\int_0^\infty p_f(z)dz}. \quad (10)$$

As is shown in the figure  $\sigma_f$  increases with  $\lambda$  (for a given network size) up to a critical value of  $\lambda$  where  $\sigma_f$  starts approaching a constant value. This behavior indicates that  $\text{CO}_2$  reached the opposite exit of the network and is a result of the finite size of the network used. Using larger networks is expected to result in shifting the critical value for  $\lambda$  to higher values.

The effect of  $\lambda$  on the mean position of the hydrate zone is shown in Fig. 9b. The dashed-dotted lines correspond to the limiting value  $X_{ft}=(N+N/10)/2$  (corresponding to the average position of the domain excluding the initial part where no hydrate forms). As  $\lambda$  increases,  $X_{ft}$  approaches the limiting value, thus indicating that  $\text{CO}_2$  reaches the opposite exit ( $j=2X_{ft}=N$ ). However, that is not the case for smaller  $\lambda$ 's because of clogging of pores (see also below). The results shown depict four different  $N \times N$  lattice sizes ( $N=100, 80, 60, 40$ ). The results for each lattice size are averaged over 80 realizations. The HSZ begins at  $j=N/10$ .

When studying systems where a reacting front propagates through the system, thus affecting the porosity/permeability of the system, emphasis should be placed on phenomena occurring at the vicinity of the front. Thus, it is useful to define transverse averages (see also Appendix for definitions). Fig. 10 shows the transversely averaged (over 80 realizations) pore-space available for  $\text{CO}_2$  flow as a function of lattice position,  $j$ ,

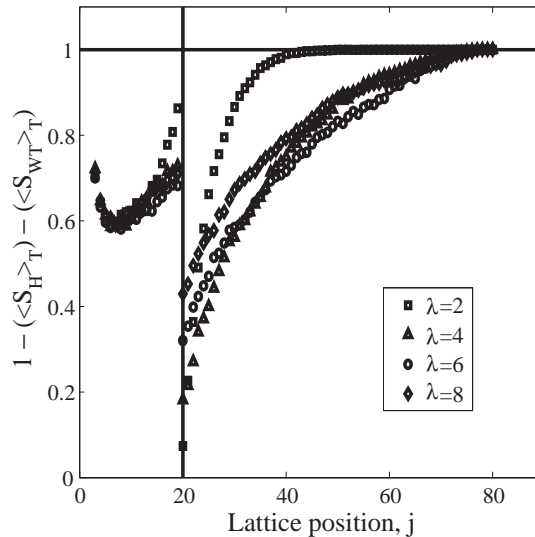


Fig. 10. Transversely averaged porosity (see Appendix for definition) available for  $\text{CO}_2$  flow as a function of lattice position,  $j$ , for an  $80 \times 80$  pore network. Results are averaged over 80 realizations.



for an  $80 \times 80$  pore network. An important observation is that even though the total porosity of the network drops due to hydrate formation, only  $\sim 5\%$ , this drop occurs in a narrow zone, close to the beginning of the HSZ, and thus blocks the pore network, inhibiting any further invasion. Results shown here are in qualitative agreement with results from Lattice Boltzmann simulations, as shown in Fig. 5. Higher  $Da_{II}$  numbers correspond to faster kinetics (recall that smaller  $\lambda$  correspond to faster kinetics for the Invasion Percolation simulations). Also from Figs. 4 and 8, we can observe similar hydrate formation patterns.

Fig. 11 shows the transversely averaged saturations (over 80 realizations) as a function of lattice position (depth of invasion),  $j$ , for an  $80 \times 80$  pore network. Results for the water

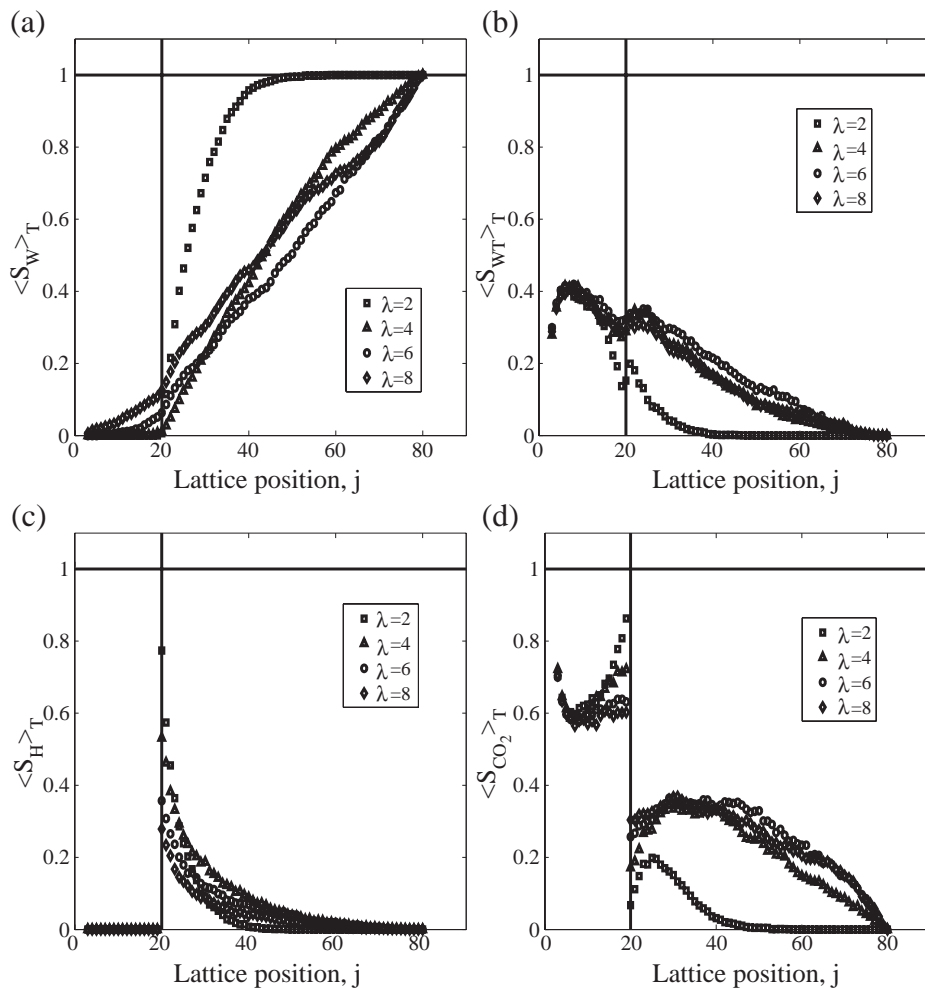


Fig. 11. Transversely averaged saturation (see Appendix for definition) as a function of lattice position,  $j$ , for an  $80 \times 80$  pore network. Results are averaged over 80 realizations.

saturation,  $\langle S_w \rangle_T$ , are shown in Fig. 11a, and for the trapped water saturation,  $\langle S_{wT} \rangle_T$ , are shown in Fig. 11b. Fig. 11c shows the results for the hydrate saturation,  $\langle S_H \rangle_T$ , and as expected higher hydrate saturations are observed for smaller  $\lambda$ 's and closer to the beginning of the HSZ. Results for the CO<sub>2</sub> saturation,  $\langle S_{CO_2} \rangle_T$  are shown in Fig. 11d. Note that for the case of  $\lambda=2$ , the CO<sub>2</sub> saturation drops to zero after invading about 20 lattice units from the beginning of the HSZ. That clearly shows that the process ends, due to hydrate blocking, before the invading CO<sub>2</sub> front reaches the opposite end at  $j=N$ . In order to observe similar behavior for higher values of  $\lambda$ 's, larger lattice sizes are required. The lattice position where the HSZ begins is located at  $j=20$  and is denoted by the vertical line.

#### 4. Summary of results

In this work, we have utilized two pore-scale methods, LB and IP in pore networks, to numerically simulate hydrate formation both from a single-phase supersaturated solution in a 2D constructed medium, and from the two-phase immiscible displacement of seawater by liquid CO<sub>2</sub>. We examined the obtained hydrate deposition patterns and changes in porosity and permeability due to hydrate formation, and how these properties depend on various parameters including a parametric study of hydrate formation kinetics. We also upscaled the pore-scale results to obtain constitutive relations for porosity, both transverse and for the entire domain, and for permeability.

It was shown that in the case of fast kinetics, the transverse porosity at the vicinity of the hydrate formation front drops significantly due to hydrate formation, essentially inhibiting any further invasion of the CO<sub>2</sub> into the sediments and resulting in a finite macroscale porosity value even when the permeability vanishes. In this case, the constitutive relation derived was quite different from the usual power-law relations often used in continuum formulations in which the permeability goes to zero at zero porosity and clogging effects are not taken into account. In the case of slower kinetics, further penetration is possible. This finding has significant meaning on the estimate of the CO<sub>2</sub> storage capacity of the oceanic sediments. Additional detailed work is required for the application of the methodologies to real oceanic sediments.

#### Acknowledgments

This work was partially supported by LDRD-DR 20030059DR and LDRD-DR 20040042DR projects, funded by Los Alamos National Laboratory, which is operated by the University of California for the U. S. Department of Energy.

#### Appendix A

Here, we introduce the definition of certain parameters used in the discussion of the results. We denote with subscript  $p(H, CO_2)$  the different phases present in the network. We further differentiate between non-trapped water ( $W$ ) and trapped water ( $WT$ ). So, in

general, we can define the overall average (denoted by  $\langle S_p \rangle$ ) and the  $j^{\text{th}}$ -row transverse average (denoted by  $\langle S_p \rangle_T(j)$ ) for the saturation of phase  $p$ , respectively, as follows:

$$\langle S_p \rangle = \frac{\sum_{j=1}^{j=M} \sum_{i=1}^{i=N} W_p(i,j) \text{ site } (i,j)}{\sum_{j=1}^{j=M} \sum_{i=1}^{i=N} \text{site } (i,j)} = \frac{\sum_{j=1}^{j=M} \sum_{i=1}^{i=N} W_p(i,j) \text{ site } (i,j)}{M \times N}, \quad (11)$$

and

$$\langle S_p \rangle_T(j) = \frac{\sum_{i=1}^{i=N} W_p(i,j) \text{ site } (i,j)}{\sum_{i=1}^{i=N} \text{site } (i,j)} = \frac{\sum_{i=1}^{i=N} W_p(i,j) \text{ site } (i,j)}{N}, \quad (12)$$

where  $\text{site } (i,j)=1$  for all sites that belong to the network and  $W_p(i,j)$  is a phase function defined as follows:

$$W_p(i,j) = \begin{cases} 1: & \text{if site } (i,j) \text{ contains phase } p \\ 0: & \text{otherwise} \end{cases}. \quad (13)$$

## References

- [1] P. Englezos, Industrial & Engineering Chemistry Research 32 (1993) 1251.
- [2] E.D. Sloan, Clathrate Hydrates of Natural Gases, 2nd edition, Marcel Dekker, New York, 1998.
- [3] B. Tohidi, R. Anderson, M.B. Clennell, R.W. Burgass, A.B. Biderkab, Geology 29 (2001) 867.
- [4] R.L. Kleinberg, C. Flaum, D.D. Griffin, P.G. Brewer, G.E. Malby, E.T. Peltzer, J.P. Yesinowski, Journal of Geophysical Research 108 (2003) 2508.
- [5] S. Chen, G.D. Doolen, Annual Review of Fluid Mechanics 30 (1998) 329.
- [6] J. Feder, Fractals, Plenum, New York, 1988.
- [7] M. Sahimi, Flow and Transport in Porous Media and Fractured Rock: From Classical Methods to Modern Approach, VHC, Weinheim, 1995.
- [8] Q. Kang, D. Zhang, S. Chen, X. He, Physical Review E 65 (2002) 036318.
- [9] Q. Kang, D. Zhang, S. Chen, Journal of Geophysical Research 108 (2003) 2505.
- [10] Q. Kang, D. Zhang, P.C. Lichtner, I.N. Tsimpanogiannis, Geophysical Research Letters 31 (2004) L21604.
- [11] I. Fatt, Transactions of AIME 207 (1956) 144.
- [12] M.J. Blunt, SPE Journal 2 (1997) 70.
- [13] M.J. Blunt, M.D. Jackson, M. Piri, P.H. Valvante, Advances in Water Research 25 (2002) 1069.
- [14] X. Li, Y.C. Yortsos, AIChE Journal 41 (1995) 214.
- [15] A. Dominguez, S. Bories, M. Prat, International Journal of Multiphase Flow 26 (2001) 1951.
- [16] M. Prat, International Journal Multiphase Flow 21 (1996) 875.
- [17] A.G. Yiotis, A.G. Boudouvis, A.K. Stubos, I.N. Tsimpanogiannis, Y.C. Yortsos, Physical Review E 68 (2003) 010310.
- [18] C. Satik, Y.C. Yortsos, ASME Journal of Heat Transfer 118 (1996) 455.
- [19] C. Du, Y.C. Yortsos, Transport in Porous Media 35 (1999) 205.
- [20] I.N. Tsimpanogiannis, Y.C. Yortsos, Journal of Colloid and Interface Science 270 (2004) 388.
- [21] Y. Qian, D. d'Humieres, P. Lallemand, Europhysics Letters 17 (1992) 479.

- [22] H. Chen, S. Chen, W.H. Matthaeus, *Physical Review A* 45 (1992) R5339.
- [23] S.P. Dawson, S. Chen, G.D. Doolen, *J. Chem. Phys.* 98 (1993) 1514.
- [24] P. Englezos, N. Kalogerakis, P.D. Dholabhai, P.R. Bishnoi, *Chemical Engineering Science* 42 (1987) 2647.
- [25] P.R. Bishnoi, V. Natarajan, *Fluid Phase Equilibria* 117 (1996) 168.
- [26] D. Wilkinson, J.F. Willemsen, *Journal Physics A* 16 (1983) 3365.
- [27] D. Wilkinson, *Physical Review A* 30 (1984) 520.
- [28] B. Sapoval, M. Rosso, J.F. Gouyet, *Journal Physique (France) Letters* 46 (1985) L119.
- [29] I.N. Tsimpanogiannis, P.C. Lichtner, *SPE Paper* 90743 (2004).
- [30] H. Teng, A. Yamasaki, *Energy Conversion Management* 39 (1998) 1045.
- [31] NIST webpage: <http://webbook.nist.gov>.
- [32] A. Hebach, A. Oberhof, N. Dahmen, A. Kogel, H. Ederer, E. Dinjus, *Journal of Chemical and Engineering Data* 47 (2002) 1540.
- [33] Y. Yang, A.C. Alpin, *Marine Petroleum Geology* 15 (1998) 163.
- [34] M.M. Dias, D. Wilkinson, *Journal of Physics. A, Mathematical and General* 19 (1986) 3131.
- [35] J. Hoshen, R. Kopelman, *Physical Review, B* 14 (1977) 1455.
- [36] G.T. Mac Donald, *Climatic Change* 16 (1990) 247.
- [37] M.B. Clennell, M. Hovland, J.S. Booth, P. Henry, W.J. Winters, *Journal of Geophysical Research* 104 (1999) 22985.
- [38] W.F. Waite, W.J. Winters, D.H. Mason, *American Mineralogist* 89 (2004) 1202.
- [39] G. Damkohler, *Zeitschrift fur Elektrochemie* 42 (1936) 846.